Elucidating the Effect of Iron Doping on the Electrochemical Performance of Cobalt-Free Lithium-Rich Layered Cathode Materials

Fanglin Wu, Guk-Tae Kim,* Matthias Kuenzel, Huang Zhang, Jakob Asenbauer, Dorin Geiger, Ute Kaiser, and Stefano Passerini*

The eco-friendly and low-cost Co-free $Li_{1.2}Mn_{0.585}Ni_{0.185}Fe_{0.03}O_2$ is investigated as a positive material for Li-ion batteries. The electrochemical performance of the 3 at% Fe-doped material exhibits an optimal performance with a capacity and voltage retention of 70 and 95%, respectively, after 200 cycles at 1C. The effect of iron doping on the electrochemical properties of lithium-rich layered materials is investigated by means of in situ X-ray diffraction spectroscopy and galvanostatic intermittent titration technique during the first charge–discharge cycle while high-resolution transmission electron microscopy is used to follow the structural and chemical change of the electrode material upon long-term cycling. By means of these characterizations it is concluded that iron doping is a suitable approach for replacing cobalt while mitigating the voltage and capacity degradation of lithium-rich layered materials. Finally, complete lithium-ion cells employing $Li_{1.2}Mn_{0.585}Ni_{0.185}Fe_{0.03}O_2$ and graphite show a specific energy of 361 Wh kg^{-1} at 0.1C rate and very stable performance upon cycling, retaining more than 80% of their initial capacity after 200 cycles at 1C rate. These results highlight the bright prospects of this material to meet the high energy density requirements for electric vehicles.

1. Introduction

Lithium-rich materials provide the highest specific energies (up to 900 Wh kg^{-1}) among all lithium-ion positive electrode materials.[1] Potentially meeting the high requirements for automotive applications, they receive much attention for use in "next-generation" Li-ion batteries (LIBs). Their large specific capacity originates from the structural peculiarity of lithium-rich layered materials, which can be seen as mixtures of two phases, $LiMO_2$ (M = Ni, Mn, and Co, rhombohedral R-3m structure) and Li_2MnO_3 (monoclinic C2/m structure). This latter component provides additional lithium located inside the transition metal layer.[2] However, to access this additional capacity, the Li_2MnO_3 component must be "activated" by charging to relatively high cut-off voltages (i.e., 4.6–4.8 V).[1a,3] During such activation, Li$^+$ ions are extracted from the structure while oxygen anion redox activity occurs possibly through a few different processes. However, transition metal migration into the formed Li vacancies correspondingly

occurs, finally resulting in the phase transformation from layered to spinel-like and eventually, rock-salt structure.[4] This is widely regarded as the origin of the two main challenges of lithium-rich materials, that is, voltage and capacity degradation, leading to relatively poor cycle-life. To solve these issues, many strategies have been developed over the past years, which are, for example, modifications of the binder[5] or the electrolyte,[6] and surface treatments[4,7] and lattice doping[8] of the lithium-rich materials.

Lattice doping is one of the most suitable methods to address the voltage fading as reported in a few earlier works. Nayak et al.[8b] could maintain higher specific capacity as well as discharge voltage upon cycling, by doping the structure with aluminum (on the account of manganese). This is due to the stabilized surface of the active material and suppressed transformation from layered to spinel-like phase. Chromium has also been adopted as a possible dopant and confirmed to be incorporated into the crystal lattice. It enabled higher average voltage, which was ascribed to a decreased amount of spinel domains generated upon cycling.[9] Moreover, other elements, such as Ti,[10] Mg,[11] and Cu[12] were investigated leading to similar improvements. Besides doping into the transitional metal layer, also lithium site

F. Wu, Dr. G.-T. Kim, M. Kuenzel, Dr. H. Zhang, J. Asenbauer,
Prof. S. Passerini
Helmholtz Institute Ulm (HIU)
Helmholtzstrasse 11, 89081 Ulm, Germany
E-mail: guk-tae.kim@kit.edu; stefano.passerini@kit.edu
F. Wu, Dr. G.-T. Kim, M. Kuenzel, Dr. H. Zhang, J. Asenbauer,
Prof. S. Passerini
Karlsruhe Institute of Technology (KIT)
P.O. Box 3640, 76021 Karlsruhe, Germany
Dr. D. Geiger, Prof. U. Kaiser
Central Facility for Electron Microscopy
Ulm University
Albert-Einstein-Allee 11, D-89081 Ulm, Germany
The ORCID identification number(s) for the author(s) of this article can be found under https://doi.org/10.1002/aenm.201902445.

**ADVANCED
SCIENCE NEWS**
www.advancedsciencenews.com

**ADVANCED
ENERGY
MATERIALS**
www.advenergymat.de

doping by alkali elements, such as Na and K, appears to be beneficial. Qing et al.[8a] introduced a novel gradient surface doping method, where Na$^+$ ions located in the lithium layer are sought to increase the kinetics of a lithium-rich cathode, achieving specific capacity of 286 mAh g^{-1} at 25 mA g^{-1}. The material displayed a good cycling stability and superior rate capacity ascribed to a pinning effect of the Na$^+$ ions to stabilize the structure and accelerate Li$^+$ diffusion, thus enhancing the material's electronic and ionic conductivities. Li et al.[13] successfully synthesized K$^+$-doped lithium-rich cathode from a potassium-containing α-MnO$_2$ source. The resulting material showed excellent cycling stability with 85% retention of the first discharge capacity (315 m Ah g^{-1}) after 110 cycles. Potassium ions have a larger ionic radius (K$^+$: 1.38 Å, Na$^+$: 1.02 Å, Li$^+$ 0.76 Å) and thus, could act as pillars, preventing the formation of tri-vacancies in the lithium layer and hinder manganese migration preventing the spinel-like phase formation. Therefore, small amounts of other alkali metals in the lithium layer can clearly contribute to mitigate voltage fading by restraining the structural transformation of the transition metal layer during cycling.

On the other hand, cobalt, one of the key constituents of conventional layered electrode materials faces a severe shortage due to the rapidly increasing demand for plug-in and full electric vehicles. According to estimates based on the current battery market development, the required amount of cobalt by 2050 would be twice as today's identified reserves.[14] Moreover, cobalt is rated highly critical regarding its health, ecological and economic impact. The heavy mining of cobalt causes harm to the people and the environment, causing inconvenience for battery manufacturers and users.[15] Therefore, the development of cobalt-free cathode materials has become an urgent matter. Toward this end, iron appears as a very appropriate candidate to replace cobalt, owing to its natural abundance low cost and environmentally friendliness. Furthermore, it is particularly suitable from the electrochemical point of view as its metal oxygen covalent bonding energy allows for the facile activation of the material, being in a similar range as other transition metal ions, that follow the order Co > Ni > Fe > Cr > Mn > Ti.[16] Recently, several groups have started to follow this approach doping lithium-rich materials with iron. Li et al.[17] investigated different contents of iron replacing cobalt in Li$_{1.2}$Mn$_{0.56}$Ni$_{0.16}$Co$_{0.08}$O$_2$, improving the achieved capacity over the pristine material. Similarly, Nayak et al.[18] investigated the effect of iron doping to suppress the discharge voltage decay and improve the cycling stability of Li$_{1.2}$Mn$_{0.56}$Ni$_{0.16}$Co$_{0.08}$O$_2$. Liu et al.[19] used iron to replace both manganese and nickel in cobalt-free Li$_{1.2}$ Mn$_{0.6}$Ni$_{0.2}$O$_2$ and showed that the Fe-doped material exhibits better cycling stability and rate capability. However, a deeper understanding of the iron doping into Li-rich layered electrode materials is still missing. Accordingly, herein we focus on investigating how the iron doping influences the material from a structural point of view and how this translates into the observed performance improvement for lithium-rich layered oxide electrodes.

2. Results and Discussion

Figure 1a shows the powder X-ray diffraction (XRD) patterns of various Fe-doped lithium-rich materials. The obtained phase can

be indexed as the hexagonal layered α-NaFeO$_2$ structure with space group R-3m. The weak reflections in the range of 20°–25° originate from the pronounced lattice ordering of Li and Mn in the transition metal (TM) layer of Li$_2$MnO$_3$ (C2/m space group). Figure 1b,c shows magnifications of the (003) and (104) reflections, respectively, highlighting the effect of iron doping on the materials structure. Upon Fe-doping both reflections shift to lower 2θ values, which is more pronounced for the 3 and 5 at% Fe-doped samples. This indicates a larger interplanar spacing for increasing iron contents, which is expected to improve the diffusion of Li$^+$ ions in the structure and, thus, to enhance the rate capability of the material. For a detailed comparison, the calculated lattice parameters are summarized in Table S1 (Supporting Information). Both the c/a and I_{003}/I_{104} ratios increase in the doped materials with respect to the pristine one, indicating that iron doping additionally reduces the cation mixing. This is expected to help suppressing the TM ions migration into the lithium layer, which is known to initiate the detrimental phase transformation.[20] The inductively coupled plasma (ICP) results summarized in Table S2 (Supporting Information) confirm that the composition of the synthesized lithium-rich materials is close to the targeted stoichiometries. Moreover, the elemental mapping obtained from energy-dispersive X-ray (EDX) spectroscopy (Figure 1d) reveals that the main elements (O, Mn, Ni, Fe) are uniformly distributed in Li$_{1.2}$Mn$_{0.6-x/2}$Ni$_{0.2-x/2}$Fe$_x$O$_2$ ($x = 0$, 0.01, 0.03, 0.05; hereinafter named LRNM). The oxidation state of iron was determined to be +3 (Fe^{3+}) by means of X-ray photoelectron spectroscopy (XPS) analysis (Figure S1, Supporting Information). The scanning electron microscopy (SEM) image of the 3 at% Fe-doped material shows that it is constituted of agglomerates of many, but rather small, primary particles.

Figure 2 compares the electrochemical performance of Fe-doped LRNMs with that of the pristine material. The initial discharge capacity of the 1 at% Fe-doped material increased slightly from 192 to 197 mAh g^{-1}. Interestingly, a significantly larger improvement can be observed for 3 and 5 at% Fe-doped samples, exhibiting first-cycle discharge capacities of 232 and 231 mAh g^{-1}, respectively. This increase is due to the Fe^{3+}/Fe^{4+} redox activity (around 4 V) during the initial cycles at 0.1C.[16] Tetravalent Fe, however, is rather unstable. Upon cycling, it transforms into the electrochemically inactive LiFeO$_2$ phase,[21] which might assist in preventing the Ni^{2+} migration from the transition metal layer to the lithium layer. Therefore, the capacity fading of 3 and 5 at% Fe-doped LRNMs is more pronounced at the beginning, but stabilizes upon cycling.[16] The capacity retention of the four materials after 200 cycles is about 60.4, 60.6, 69.6, and 66.4% for $x = 0$, 0.01, 0.03, and 0.05, respectively, indicating the best cycling stability for the 3 at% Fe-doped material (Figure 2a). The rate capability of the same materials was also evaluated, once more revealing the 3 at% Fe-doped LRNM (Figure 2b) as the best performing, combining the largest interlayer spacing (see Table S1, Supporting Information) with the intermediate content of Fe (which becomes inactive upon cycling).[16,21]

Considering the commercial application of the lithium-rich cathode materials, the impact of voltage fading on the energy density is a more serious concern than that of capacity fading.[22] **Figure 3** shows a few, selected charge–discharge potential profiles of pristine and 1, 3, and 5 at% Fe-doped LRNMs recorded at 1C. Clearly, the voltage fading is less severe for the 3 and
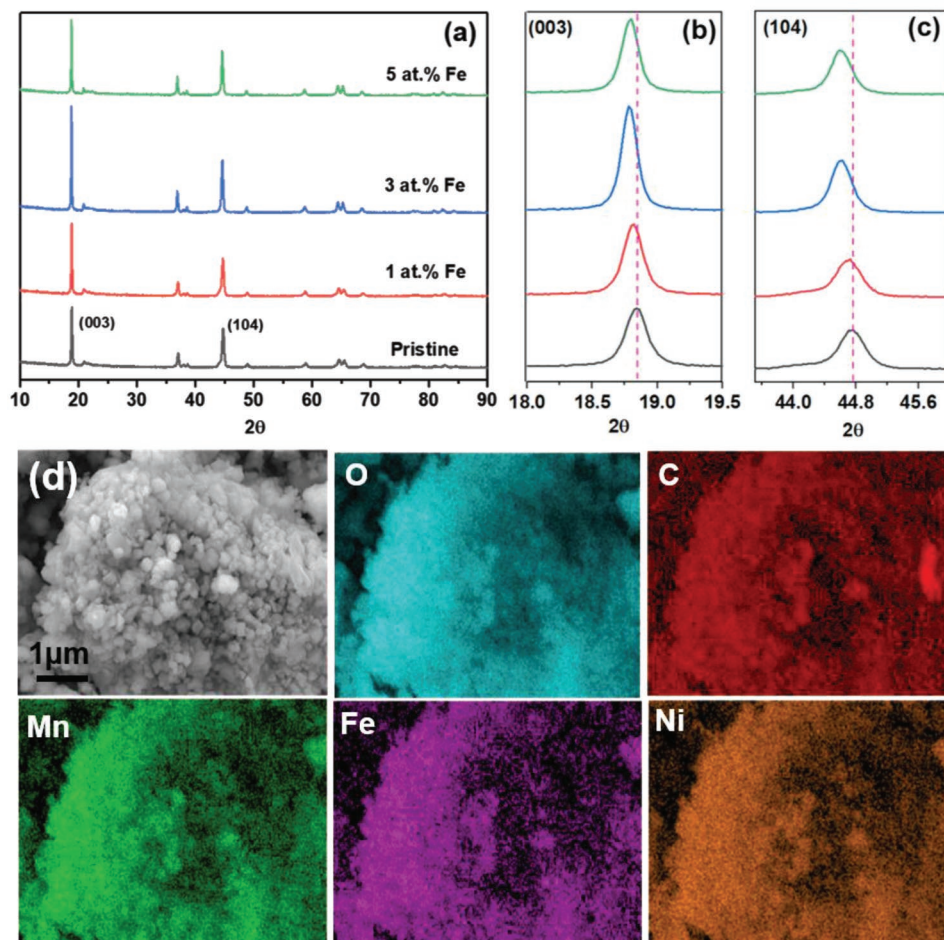
Figure 1. a) XRD patterns of pristine and 1, 3, and 5 at% Fe-doped LRNMs. b,c) Magnifications for the (003) and (104) reflections are also provided. d) SEM image and corresponding EDX elemental mapping of O, C, Mn, Fe, and Ni of the 3 at% Fe-doped sample.

5 at% Fe-doped samples. For a better comparison among the materials, the average discharge voltage obtained from the potential profiles is depicted in **Figure 4**. Comparing the 3rd and 208th cycles, the mean discharge voltage drops from 3.54 to 3.24 V ($\Delta E = 0.30$ V) in the pristine material and, similarly, from 3.54 to 3.27 V ($\Delta E = 0.27$ V) in the 1 at% Fe-doped material. However, for the materials with 3 and 5 at% Fe-doping the voltage decay is only 0.17 and 0.21 V, respectively. Therefore, the voltage fading of LRNM can be clearly reduced by substituting cobalt with iron, in good agreement with a previous study.[18]

Thus far, only the beneficial effect of iron doping to improve the capacity and mitigate the voltage fading of LRNMs during cycling
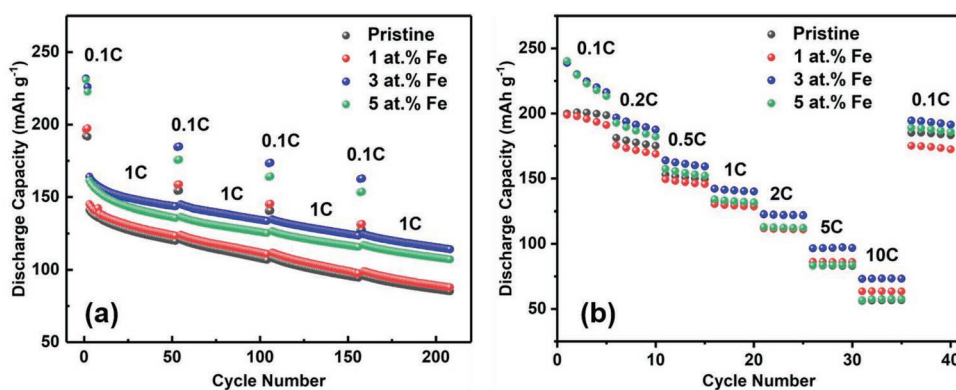
Figure 2. a) Constant current discharge/charge cycling and b) rate capability of pristine and 1, 3, and 5 at% Fe-doped LRNMs. The 1C rate corresponds to a specific current of 250 mA g^{-1}. All tests were performed at 20 °C.
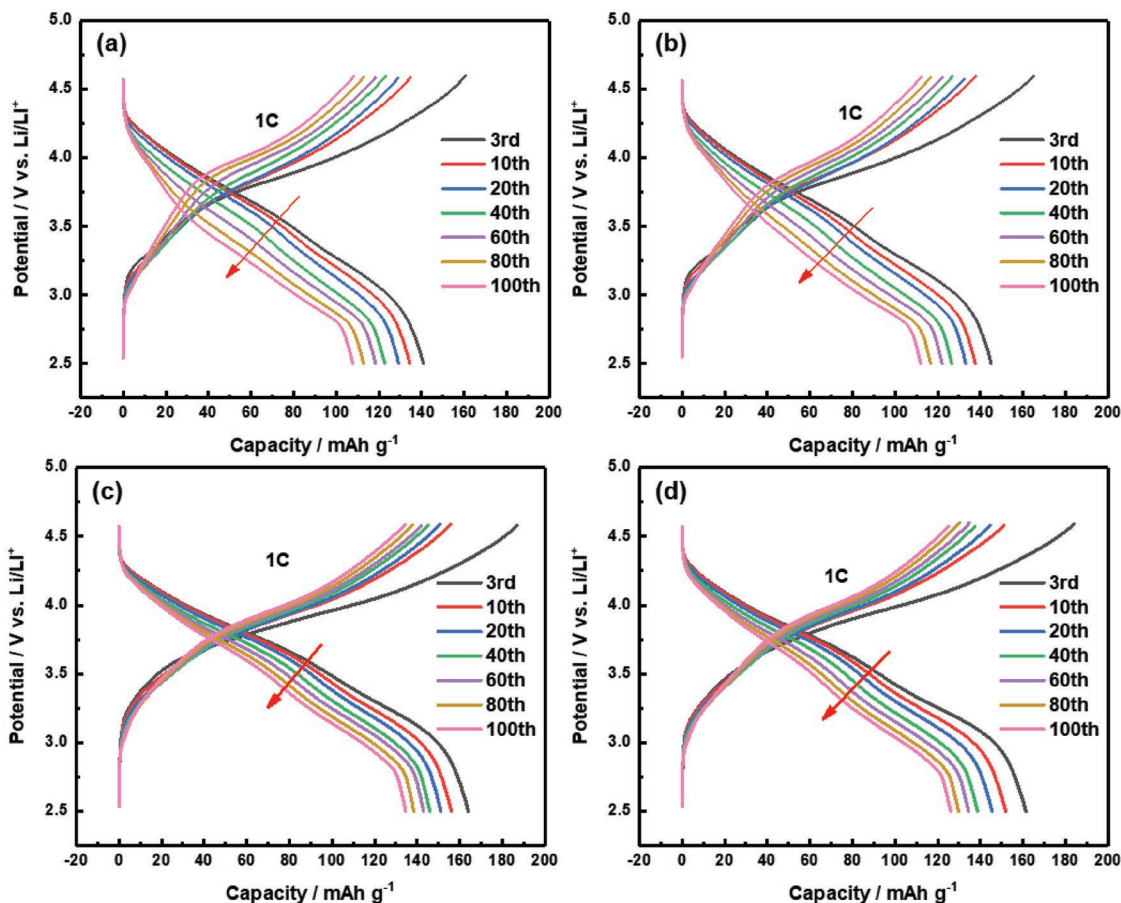
Figure 3. a–d) Selected potential profiles of the pristine, 1, 3, and 5 at% Fe-doped materials upon constant discharge/charge cycles at 1C rate.

has been presented. However, the activation of the Li_2MnO_3 component at high voltage (around 4.6 V) during the first charge is vital for the performance of LRNMs.[3b] Hence, the investigation
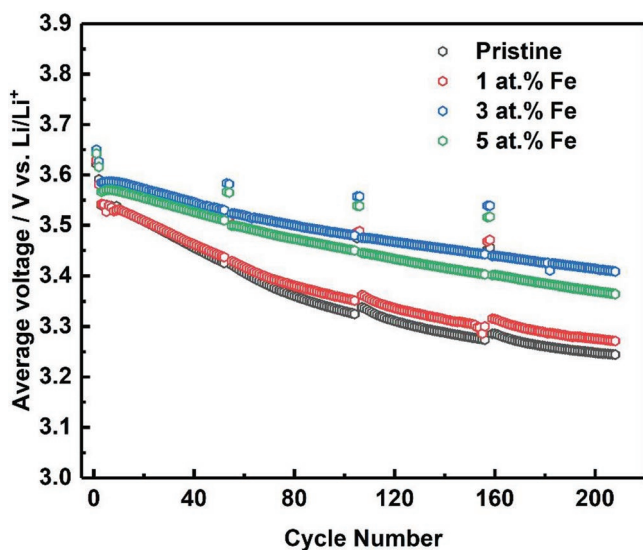
Figure 4. Average discharge voltage over cycling of pristine and 1, 3, and 5 at% Fe-doped LRNMs.

focused on the impact of iron doping on the first charge–discharge cycle in more detail, to correlate the structural changes introduced by the dopant to the improved electrochemical behavior. The in situ XRD data in **Figure 5** nicely allow to follow the structural transformation occurring in the 3 at% Fe-doped material, that is, the best performing one, upon its activation (up to 4.8 V) during the first charge. The whole cycle can be divided into three regions. Region I ranges from OCV to roughly 4.4 V, which is the endpoint of the first sloping part in the potential profile. During this step the (104) peak shifts to higher 2θ values, while the splitting of the (108)/(110) reflections increases simultaneously. This means that the distance between the transition metal layers is decreasing, mainly resulting from the oxidation of Ni^{2+} (0.69 Å) to Ni^{4+} (0.48 Å) upon Li^+ extraction. In the plateau of Region II, that is, until the end of charge, however, the (104) peak as well as the (108)/(110) reflections remain nearly unchanged, indicating that no more Li^+ is extracted from the transition metal layer. Therefore, the capacity originates from the activation of the Li_2MnO_3 component. During the lithiation (discharge) process in Region III, these peaks shift back to their initial positions confirming the reversible reduction of Ni^{4+} to Ni^{2+} accompanied by reinsertion of Li^+ into the transition metal layers.[23]

For a closer comparison of the activation behavior of the four LRNM materials doped with different amounts of iron, the first charge/discharge potential profiles are shown in

ADVANCED
SCIENCE NEWS
www.advancedsciencenews.com

ADVANCED
ENERGY
MATERIALS
www.advenergymat.de
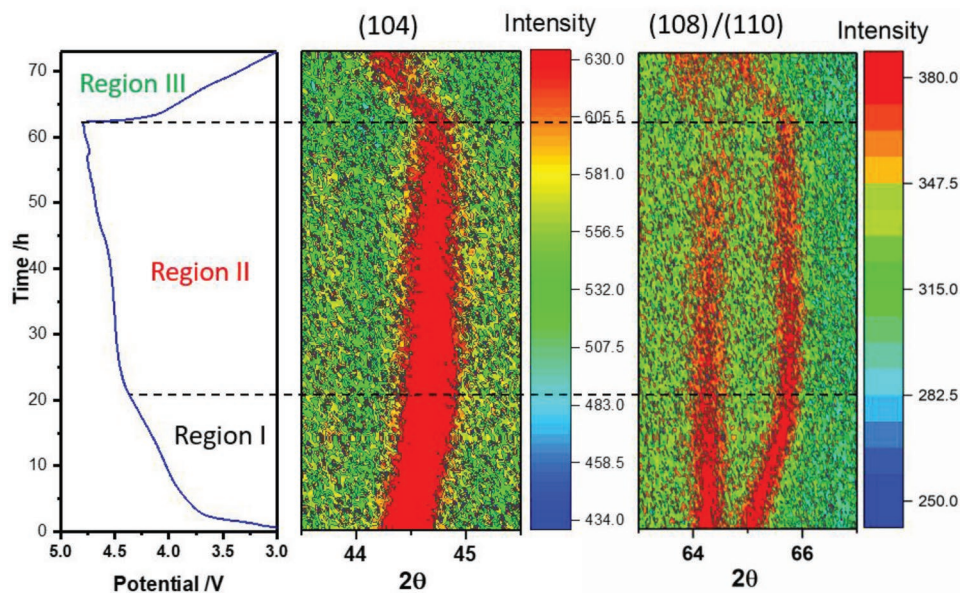
Figure 5. In situ XRD analysis of the 3 at% Fe-doped material during the first charge/discharge (delithiation/lithiation) process within the 3.0–4.8 V voltage window. Charge current: 20 µA; discharge current: 50 µA. The corresponding contour graphs of the (104) and (108)/(110) reflections are shown.

Figure 6. The black lines divide the first charge into two parts: a sloping region up to 4.4 V and the plateau region until end of charge. By introducing iron into the structure the capacity of the sloping region associated to transition metal oxidation is clearly enhanced, particularly for the 3 and 5 at% Fe-doped materials. This can be attributed to the oxidation of Fe^{3+} to Fe^{4+} occurring at about 4.0 V as iron is occupying sites in the transition metal layer.[16] However, at the same time the capacity of the plateau region is lower than that of the pristine and 1 at% LRNMs, indicating a suppressed oxygen loss from the Li_2MnO_3 component.[16] Moreover, the first cycle coulombic efficiency increases in the order 67.6, 69.3, 77.5, and 79.0%, with increasing iron content pointing toward the iron doping suppressing the cation mixing in the LRNM. In fact, although Li^+ can be extracted more easily from both the lithium and transition metal layer for high cation mixing levels, it is less favorably reinserted into the lithium layer,[24] thus lowering the coulombic efficiency. Therefore, the iron doping contributes to improve the coulombic efficiency and specific capacity of LRNMs by suppressing oxygen release and, thus, Ni^{2+} migration into the Li layer during the first cycle activation.[3,25]

To further correlate the structural changes induced by Fe-doping of LRNMs, that is, the suppression of cation mixing and the increased interlayer spacing, the lithium transfer kinetics were investigated in more detail. For this purpose the apparent Li^+ ion diffusion coefficient was obtained by performing cyclic voltammetry measurements at different scan rates (see Figure S2, Supporting Information) and analyzing the peak current density, Ip, according to Randles–Sevcik equation[26]

$$Ip = 2.68 \times 10^5 n^{3/2} A D^{1/2} C \omega^{1/2}$$

where n is the number of electrons transferred during the redox reaction, A is the electrode area (1.13 cm^2), D is the
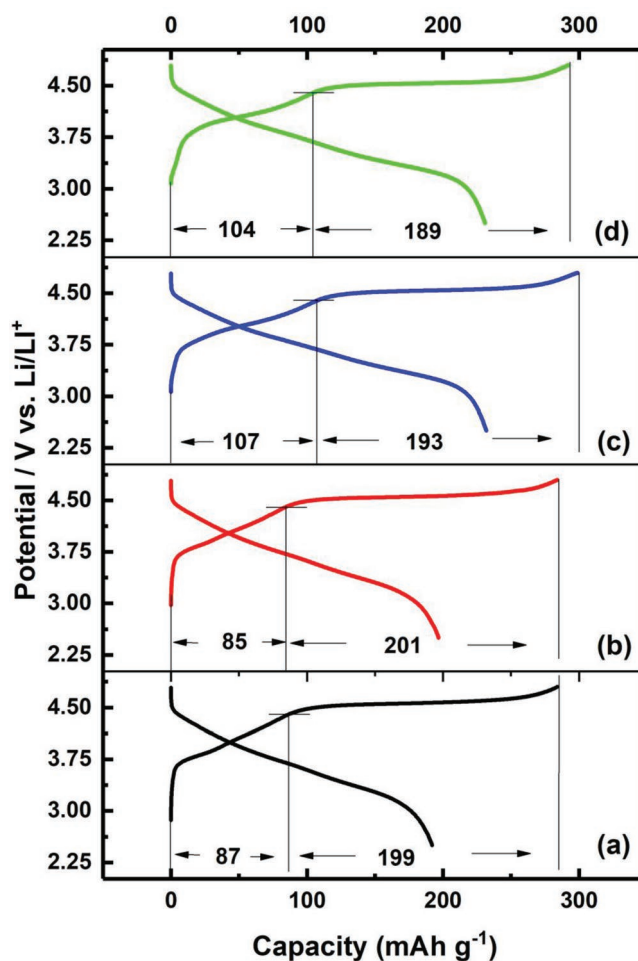
Figure 6. a–d) Comparison of the first cycle potential profiles of pristine, 1 at%, 3 at%, and 5 at% Fe-doped materials at a discharge/charge rate of 0.1C.
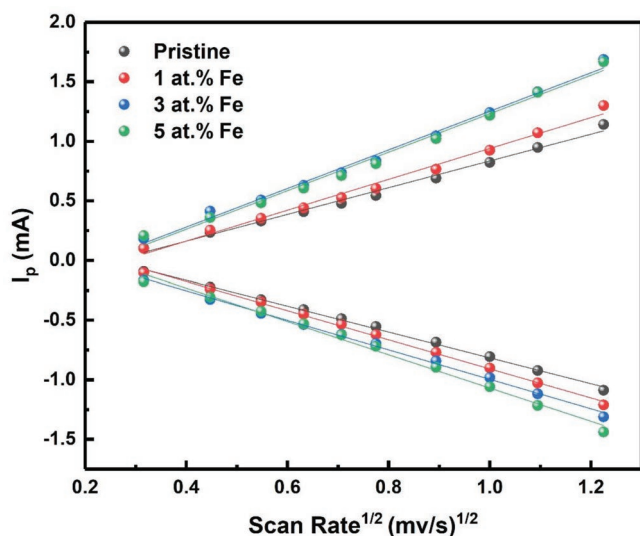
Figure 7. Randles–Sevcik analysis of the peak current density against the square root of increasing scan rates during cyclic voltammetry (see Figure S2, Supporting Information) of the four materials with different iron content.

apparent Li$^+$ diffusion coefficient, C is the molar concentration of Li$^+$ in the LRNM, and ω is the scan rate (mV s^{-1}). Although it is not appropriate for the absolute determination of the D, the geometric electrode area was used because the results are only used to compare rather similar materials in terms of morphology and surface area processed into electrodes following the same procedure. Directly from Figure S2 (Supporting Information), it is evident that the features around 4.0 V (charge) and 3.6 V (discharge) were more pronounced for the 3 and 5 at% Fe-doped materials as compared to the pristine one. These two peaks show a linear relationship between peak current intensity and the square root of the scan rate; thus, they can be used to obtain the apparent Li$^+$ ion diffusion coefficient. The detailed values are summarized in Table S3 (Supporting Information), but from **Figure 7** it is evident from that the D_{Li+} value of all Fe-doped samples are larger than that of the pristine material. This further confirms the enhanced lithium-ion diffusion and transfer kinetics achieved through lattice doping with iron.

Furthermore, the galvanostatic intermittent titration technique (GITT) was employed to follow the Li$^+$ diffusion kinetics during the activation of the various Fe-doped materials, that is, the very first charge process, which is significantly different from the subsequent cycles.[27] The results of the GITT experiment comparing the pristine and 3 at% Fe-doped LRNM materials are displayed in **Figure 8**. In general, the small current pulse applied and the extended rest interval between two consecutive pulses should be sufficient to reach a

steady state during relaxation of the voltage. Unfortunately, this is not true for LRNM materials during the first charge process, because of the sluggish kinetics, as also reported by Li et al.[28] Even applying rather low pulse current (C/20 rate) and allowing for a relaxation period of 4 h, altogether corresponding to a C/100 charge time, steady-state conditions were not achieved during the GITT measurements. Nevertheless, it is still possible to draw conclusions of a more qualitative nature by comparing the recorded curves. The voltage response of both materials is nearly identical below 4.0 V. However, in the region between 4.0 and 4.4 V the voltage of the pristine material increases faster than that of the 3 at% Fe-doped one. This indicates an increased internal resistance for the pristine sample and again confirms that Li$^+$ diffusion is more facile in the 3 at% Fe-doped LRNM. Above 4.4 V, both curves approach each other and nearly converge again. Nevertheless, when enlarging the response for an individual impulse (see inset in Figure 8), it is evident that polarization is significantly more severe for the pristine sample compared to the 3 at% Fe-doped material. Additionally, the relaxation observed during the rest step tends to be faster for the doped material, which can be attributed to higher Li$^+$ diffusion, also during the high-voltage activation step, by doping iron into the LRNM structure.[28]

To eventually elucidate and visualize the impact of iron doping on the structure of LRNMs, a detailed investigation by means of high-resolution transmission electron microscopy (HRTEM) was conducted on the pristine and 3 at% Fe-doped materials (**Figure 9**). Both samples display a well-ordered layered structure (compare atom arrangement and corresponding fast Fourier transform (FFT) patterns in Figure 9a,b), but when measuring their lattice distances, it can be seen that the layer distance is larger in the Fe-doped material in excellent
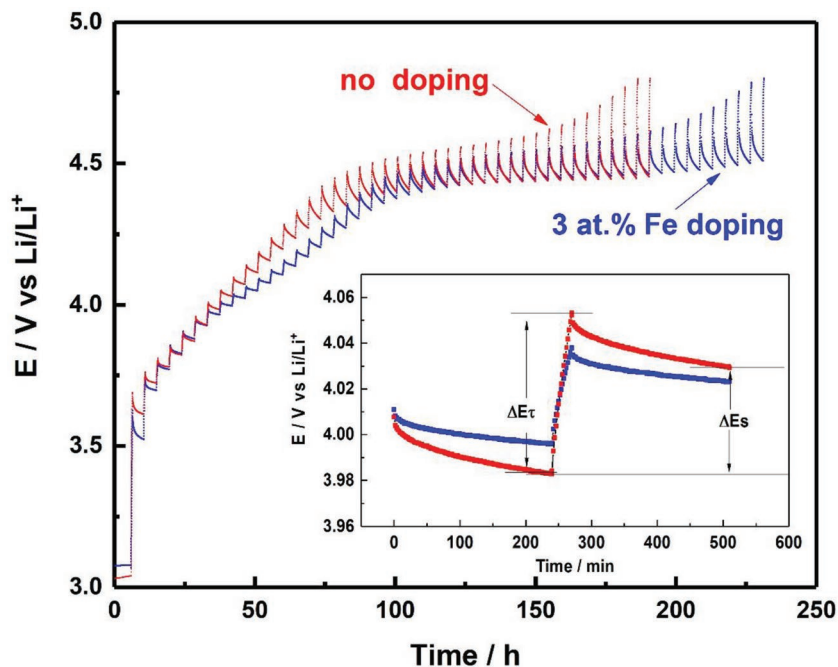
Figure 8. GITT curves of pristine (red trace) and 3% Fe-doped (blue trace) materials. The electrodes were subjected to 30 min current pulses at 12.5 mA g^{-1} (0.05C) and let to rest for 4 h between each pulse.
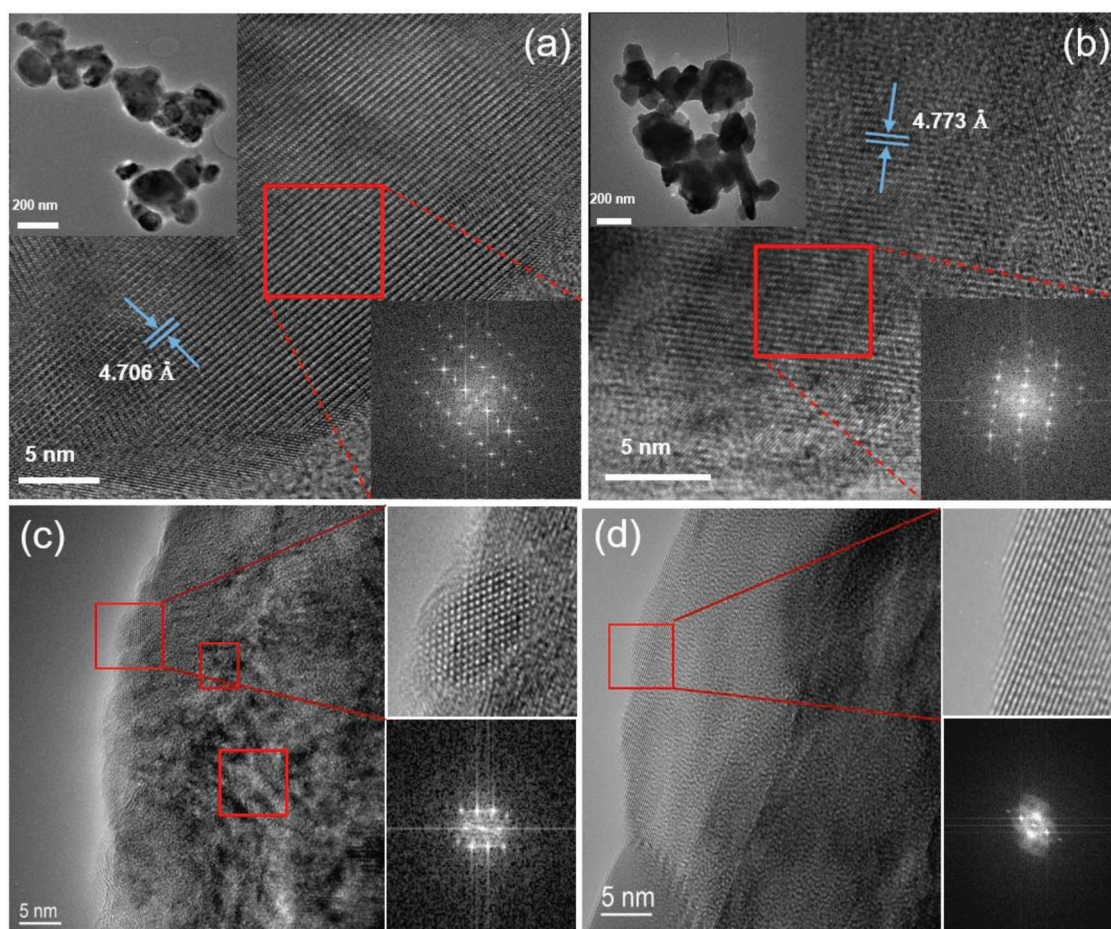
Figure 9. HRTEM images and relevant FFT patterns of a,c) pristine and b,d) 3% Fe-doped materials. Panels (a, b) and (c,d) refer to the materials before and after cycling, respectively.

agreement with the XRD results. The ionic radius of Fe^{3+} (0.645 Å) is rather similar to that of Ni^{2+} (0.69 Å), but it is much larger than that of Mn^{4+} (0.53 Å), therefore increasing the transition metal layer spacing when replacing nickel and manganese in equal shares. The HRTEM images of the pristine and 3 at% Fe-doped materials recovered from electrodes after 100 charge–discharge cycles were also investigated. Clearly, the crystal structure of the pristine sample (Figure 9c) has partially undergone transformation from a layered to rock-salt structure (NiO phase). This is caused by Ni^{2+} migration from the transition metal layer into the lithium layer during the repeated charge steps to high voltage (above 4.6 V), which is the origin of the voltage fading in LRNMs.[11a,29] However, in the microscopy images of the 3 at% Fe-doped material after cycling (Figure 9d) hardly any regions with rock-salt structure can be identified, while the layered structure is well preserved. This proves that Fe doping mitigates Ni^{2+} migration into the lithium layer, thus, explaining the decreased voltage fading and improved cycling stability observed for the Fe-doped materials.

Finally, we evaluated the electrochemical performance of the 3 at% Fe-doped material in lithium-ion full-cells, which is a crucial test for any electrode material to be potentially commercialized.[30] For this purpose, we chose graphite as the negative electrode. The resulting high energy density cell shows rather promising performance (**Figure 10**a). The first discharge capacity of 213 mAh g^{-1} (of LRNM) is, in fact, only slightly lower than that achieved in half-cell tests (232 mAh g^{-1}). Additionally, the cell displays very stable performance upon subsequent cycles. The capacity retention after 200 cycles at 1C (80.4%) is much higher than that obtained in half-cell configuration (69.4%) due to reduced electrode cross-talking. Even more promising, the coulombic efficiency well beyond 99.7% over 200 cycles is an outstanding result for a lithium-ion full-cell with a Li-rich, Co-free layered oxide positive electrode material.[31] Moreover, the specific energy density, calculated from the potential profiles, achieves a maximum value of about 361 Wh kg^{-1} at 0.1C, which is even higher than previous results concerning Co-containing, Li-rich materials; additionally, the rather promising value of 200 Wh kg^{-1} was maintained during 200 cycles at 1C, which is considered the benchmark requirement to meet for application in electric vehicles (Figure 10b). The comparison presented in Table S4 (Supporting Information) highlights the rather good, if not the best, performance of the cell herein developed with respect to the other Co-free cells reported to date.

**ADVANCED
SCIENCE NEWS**
www.advancedsciencenews.com

**ADVANCED
ENERGY
MATERIALS**
www.advenergymat.de
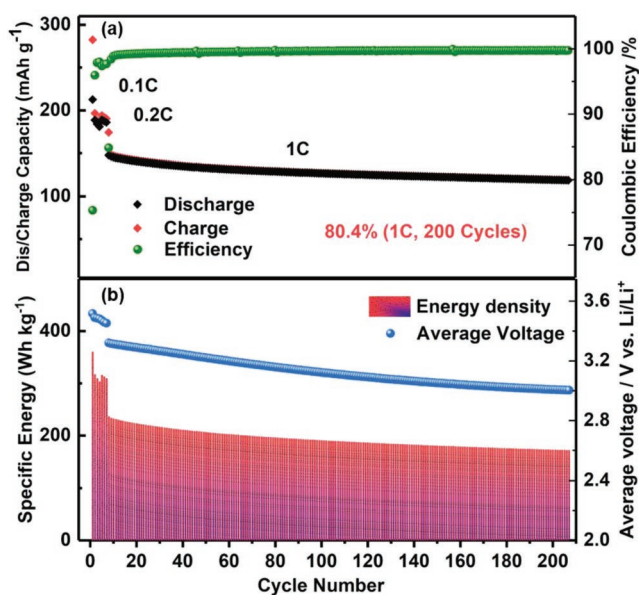
Figure 10. a) Long-term constant current cycling of a $Li_{1.2}Mn_{0.585}Ni_{0.185}Fe_{0.03}O_2$/graphite cell in the 2.3–4.7 V (1st cycle) and 2.3–4.6 V (2nd–207th cycles) voltage ranges. b) Energy density and average discharge voltage of the $Li_{1.2}Mn_{0.585}Ni_{0.185}Fe_{0.03}O_2$/graphite lithium-ion full-cell. The specific energy density was calculated based on the mass of both active materials (cathode and anode).

3. Conclusions

Herein, we demonstrated the potential of substituting cobalt through iron in LRNMs. We successfully synthesized a Co-free, LRNM by simple solid-state reaction and systematically studied the impact of Fe-doping on the structure of LRNM to explain its improved electrochemical performance. First, Fe-doping (3 at%) can offset part of the capacity loss associated to the removal of cobalt from the structure increasing the discharge capacity from 192 mAh g^{-1} in $Li_{1.2}Mn_{0.6}Ni_{0.2}O_2$ to 232 mAh g^{-1} for $Li_{1.2}Mn_{0.585}Ni_{0.185}Fe_{0.03}O_2$. Second, it dramatically reduces the capacity and voltage fading of the pristine material improving (upon 200 cycles) both the capacity retention (from 60 to 70%) and the voltage retention (from 92 to 95%). Additionally, the Fe-doping results in an increased first cycle coulombic efficiency (from 67.6 to 77.5%). Combining several structural and electrochemical characterization methods we elucidated the origin of these improvements. Iron doping into the transition metal layer increases the lattice distance, enhancing the Li$^+$ ion diffusion in the host structure. Additionally, it suppresses nickel migration into the lithium layer, hindering the crystal structure transformation from layered to spinel-like and finally rock-salt structure. By this, it also mitigates the capacity and voltage fading of the LRNM. Finally, iron is nontoxic, cheap, and environmentally friendly, particularly compared to cobalt, and, therefore, the ideal choice for its substitution in next-generation lithium-ion cathode materials.

4. Experimental Section

Synthesis: $Li_{1.2}Ni_{0.2-x/2}Mn_{0.6-x/2}Fe_xO_2$ (x = 0, 0.01, 0.03, 0.05) materials were synthesized by solid-state reaction. Stoichiometric amounts of LiCH$_3$COO (5 at% excess), Mn(CH$_3$COO)$_2$·4H$_2$O,

Ni(CH$_3$COO)$_2$·4H$_2$O, and FeSO$_4$·7H$_2$O were ball milled for 3 h and dried at 80 °C overnight. The obtained precursor was ground, then preheated at 480 °C for 5 h (3 °C min^{-1}) and pressed into pellets. The pellets were calcined in a box furnace at 900 °C for 6 h, then immediately quenched into liquid nitrogen followed by grinding and sieving to obtain the final powder.

Materials Characterization: The composition of the as-prepared materials was confirmed by inductively coupled plasma optical emission spectrometry (ICP-OES) analysis, carried out on a Spectro Arcos spectrometer (Spectro Analytical Instruments). The materials crystalline structure was characterized by XRD using a Bruker D8 Advance diffractometer (Cu Kα radiation, λ = 0.154 nm) in the 2θ range between $10° \leq 2\theta \leq 90°$. The recorded reflections were assigned to the patterns recorded using the ICDD database implemented in the EVA software (Bruker). Scanning electron microscopy was performed utilizing a Zeiss Crossbeam 340 field-emission electron microscope equipped with an EDX spectrometer (Oxford Instruments X-Max Xtreme, 100 mm^2, 1–5 kV) in order to investigate the materials morphology and composition. High-resolution transmission electron microscopy (HRTEM, Titan 80-330 kV with an image C$_s$-corrector operated at 300 kV) was employed to follow the crystal structure transformation upon pristine material and 3 at% Fe-doped material.

Electrochemical Characterization: Positive electrode (cathode) tapes were prepared by spreading a slurry containing each one of the electrode materials, conductive carbon Super C65 (IMERYS) and polyvinylidene difluoride (PVdF, Solef 6020, Solvay) in the 85:10:5 dry ratio on aluminum foil. After predrying, disc electrodes (12 mm diameter) were punched, dried under dynamic vacuum at 120 °C for 12 h and then pressed at 8 ton cm^{-2}. The average active material areal loading was close to 2 mg cm^{-2}. The electrochemical performance was evaluated in three-electrode Swagelok-type cells assembled in an argon-filled glove box (MB200B ECO, MBraun; H$_2$O and O$_2$ content lower than 0.1 ppm). Lithium metal foils served as counter and reference electrodes and glass fiber sheets (Whatman GF/D) as separator, which were soaked with the electrolyte solution (1 M LiPF$_6$ in ethyl carbonate (EC)/dimethyl carbonate (DMC), 1:1 w/w, Selectilyte LP 30, BASF). Galvanostatic discharge/charge cycling was performed at 20 ± 2 °C utilizing a battery tester (Maccor S4300). The first two galvanostatic cycles were performed within the 2.5–4.8 V voltage range at 0.1C, while for the following cycles the cut-off voltages were 2.5 and 4.6 V and the rate was 1C. GITT was as well performed on the same kind of cells, which were charged with a constant current at 0.05C for 30 min, and then allowed to rest for 4 h during which the relaxation of the voltage was recorded. Full lithium-ion cells were tested in 2032-type coin cells in a voltage range from 2.3 to 4.6 V (2.3 to 4.7 V for 1st cycle), employing graphite (SLP30) as negative electrode, the negative electrodes were made up of graphite (90%, SLP30), Super C45 carbon (5 wt%, IMERYS), and NaCMC (5%, Walocel CRT 2000). In all these cells, the negative/positive (N/P) mass ratio about 1.05. The applied dis/charge rate of 1C corresponds, for the positive electrode material, to a specific current of 250 mA g^{-1}. All potential values given herein refer to the Li$^+$/Li quasi-reference redox couple.

In Situ XRD Measurement: In situ XRD experiments were performed in coin cells (2032) with a Kapton window on the Bruker D8 Advance diffractometer (Cu Kα radiation (λ = 0.154 nm) in the 2θ range between $10° \leq 2\theta \leq 90°$. During slow charge (20 µA) up to 4.8 V and discharge (50 µA) to 3.0 V, XRD patterns were continuously recorded every 30 min. For these tests, the cathode electrode was prepared casting the electrode slurry (same composition as above) on carbon paper (30 µm). The electrode was dried at 60 °C overnight, then cut in 12 mm diameter disk electrodes and further dried under dynamic vacuum at 120 °C for 12 h.

Supporting Information

Supporting Information is available from the Wiley Online Library or from the author.

[1] a) J. Zheng, S. Myeong, W. Cho, P. Yan, J. Xiao, C. Wang, J. Cho, J.-G. Zhang, *Adv. Energy Mater.* **2017**, *7*, 1601284; b) J. Wang, X. He, E. Paillard, N. Laszczynski, J. Li, S. Passerini, *Adv. Energy Mater.* **2016**, *6*, 1600906.

[2] a) P. Rozier, J. M. Tarascon, *J. Electrochem. Soc.* **2015**, *162*, A2490; b) M. M. Thackeray, S.-H. Kang, C. S. Johnson, J. T. Vaughey, R. Benedek, S. A. Hackney, *J. Mater. Chem.* **2007**, *17*, 3112.

[3] a) W. Li, B. Song, A. Manthiram, *Chem. Soc. Rev.* **2017**, *46*, 3006; b) E. M. Erickson, F. Schipper, T. R. Penki, J.-Y. Shin, C. Erk, F.-F. Chesneau, B. Markovsky, D. Aurbach, *J. Electrochem. Soc.* **2017**, *164*, A6341.

[4] P. Oh, M. Ko, S. Myeong, Y. Kim, J. Cho, *Adv. Energy Mater.* **2014**, *4*, 1400631.

[5] T. Zhang, J. T. Li, J. Liu, Y. P. Deng, Z. G. Wu, Z. W. Yin, D. Guo, L. Huang, S. G. Sun, *Chem. Commun.* **2016**, *52*, 4683.

[6] a) J. Zheng, J. Xiao, M. Gu, P. Zuo, C. Wang, J.-G. Zhang, *J. Power Sources* **2014**, *250*, 313; b) J. Li, S. Jeong, R. Kloepsch, M. Winter, S. Passerini, *J. Power Sources* **2013**, *239*, 490.

[7] a) C.-C. Wang, J.-W. Lin, Y.-H. Yu, K.-H. Lai, K.-F. Chiu, C.-C. Kei, *ACS Sustainable Chem. Eng.* **2018**, *6*, 16941; b) X. D. Zhang, J. L. Shi, J. Y. Liang, Y. X. Yin, J. N. Zhang, X. Q. Yu, Y. G. Guo, *Adv. Mater.* **2018**, *30*, 1801751.

[8] a) R.-P. Qing, J.-L. Shi, D.-D. Xiao, X.-D. Zhang, Y.-X. Yin, Y.-B. Zhai, L. Gu, Y.-G. Guo, *Adv. Energy Mater.* **2016**, *6*, 1501914;

b) P. K. Nayak, J. Grinblat, M. Levi, E. Levi, S. Kim, J. W. Choi, D. Aurbach, *Adv. Energy Mater.* **2016**, *6*, 1502398; c) Y. Wang, Z. Yang, Y. Qian, L. Gu, H. Zhou, *Adv. Mater.* **2015**, *27*, 3915; d) Z. Sun, L. Xu, C. Dong, H. Zhang, M. Zhang, Y. Liu, Y. Zhou, Y. Han, Y. Chen, *J. Mater. Chem. A* **2019**, *7*, 3375.

[9] B. Song, C. Zhou, H. Wang, H. Liu, Z. Liu, M. O. Lai, L. Lu, *J. Electrochem. Soc.* **2014**, *161*, A1723.

[10] X. Feng, Y. Gao, L. Ben, Z. Yang, Z. Wang, L. Chen, *J. Power Sources* **2016**, *317*, 74.

[11] a) W. Liu, P. Oh, X. Liu, S. Myeong, W. Cho, J. Cho, *Adv. Energy Mater.* **2015**, *5*, 1500274; b) W. Luo, F. Zhou, X. Zhao, Z. Lu, X. Li, J. R. Dahn, *Chem. Mater.* **2010**, *22*, 1164; c) T. F. Yi, Y. M. Li, S. Y. Yang, Y. R. Zhu, Y. Xie, *ACS Appl. Mater. Interfaces* **2016**, *8*, 32349.

[12] J.-M. Lim, T. Hwang, M.-S. Park, M. Cho, K. Cho, *Chem. Mater.* **2016**, *28*, 8201.

[13] Q. Li, G. Li, C. Fu, D. Luo, J. Fan, L. Li, *ACS Appl. Mater. Interfaces* **2014**, *6*, 10330.

[14] C. Vaalma, D. Buchholz, M. Weil, S. Passerini, *Nat. Rev. Mater.* **2018**, *3*, 18013.

[15] a) R. Schmuch, R. Wagner, G. Hörpel, T. Placke, M. Winter, *Nat. Energy* **2018**, *3*, 267; b) E. A. Olivetti, G. Ceder, G. G. Gaustad, X. Fu, *Joule* **2017**, *1*, 229.

[16] C.-C. Wang, A. Manthiram, *J. Mater. Chem. A* **2013**, *1*, 10209.

[17] T.-F. Yi, Y.-M. Li, X.-D. Cai, S.-Y. Yang, Y.-R. Zhu, *Mater. Today Energy* **2017**, *4*, 25.

[18] P. K. Nayak, J. Grinblat, M. Levi, O. Haik, E. Levi, D. Aurbach, *J. Solid State Electrochem.* **2015**, *19*, 2781.

[19] X. Liu, T. Huang, A. Yu, *Electrochim. Acta* **2014**, *133*, 555.

[20] N. N. Sinha, N. Munichandraiah, *ACS Appl. Mater. Interfaces* **2009**, *1*, 1241.

[21] M. Tabuchi, Y. Nabeshima, T. Takeuchi, H. Kageyama, K. Tatsumi, J. Akimoto, H. Shibuya, J. Imaizumi, *J. Power Sources* **2011**, *196*, 3611.

[22] S. Myeong, W. Cho, W. Jin, J. Hwang, M. Yoon, Y. Yoo, G. Nam, H. Jang, J. G. Han, N. S. Choi, M. G. Kim, J. Cho, *Nat. Commun.* **2018**, *9*, 3285.

[23] D. Mohanty, S. Kalnaus, R. A. Meisner, K. J. Rhodes, J. Li, E. A. Payzant, D. L. Wood, C. Daniel, *J. Power Sources* **2013**, *229*, 239.

[24] P. G. A. Rougier, C. Delmas, *J. Electrochem. Soc.* **1996**, *143*, 1168.

[25] C. P. Laisa, A. K. N. Kumar, S. Selva Chandrasekaran, P. Murugan, N. Lakshminarasimhan, R. Govindaraj, K. Ramesha, *J. Power Sources* **2016**, *324*, 462.

[26] X. Hou, Y. Huang, S. Ma, X. Zou, S. Hu, Y. Wu, *Mater. Res. Bull.* **2015**, *63*, 256.

[27] R. A. H. W. Weppner, *J. Electrochem. Soc.* **1977**, *124*, 1569.

[28] F. Du, Z. Li, X. Bie, D. Zhang, Y. Cai, X. Cui, C. Wang, Y. Wei, G. Chen, *J. Phys. Chem. C* **2010**, *114*, 22751.

[29] G. Chen, J. An, Y. Meng, C. Yuan, B. Matthews, F. Dou, L. Shi, Y. Zhou, P. Song, G. Wu, D. Zhang, *Nano Energy* **2019**, *57*, 157.

[30] a) P. K. Nayak, T. R. Penki, B. Markovsky, D. Aurbach, *ACS Energy Lett.* **2017**, *2*, 544; b) J. An, L. Shi, G. Chen, M. Li, H. Liu, S. Yuan, S. Chen, D. Zhang, *J. Mater. Chem. A* **2017**, *5*, 19738.

[31] X. Qin, J. Wang, Y. Mai, D. Tang, X. Zhao, L. Zhang, *Ionics* **2013**, *19*, 1567.